HHS Public Access
Author manuscript
NMR Biomed. Author manuscript; available in PMC 2020 July 01.

Published in final edited form as:
NMR Biomed. 2019 July ; 32(7): e4101. doi:10.1002/nbm.4101.

Oxygen-Sensitive MRI Assessment of Tumor Response to Hypoxic Gas Breathing Challenge*

Donghan M. Yang, **Tatsuya J. Arai**, **James W. Campbell III**, **Jenifer L. Gerberich**, **Heling Zhou**, and **Ralph P. Mason**
Department of Radiology, UT Southwestern Medical Center, Dallas, Texas, USA

Abstract

Oxygen-sensitive MRI has been extensively used to investigate tumor oxygenation based on the response (R_2* and/or R_1) to a gas breathing challenge. Most studies have reported response to hyperoxic gas indicating potential biomarkers of hypoxia. Few studies have examined hypoxic gas breathing and we have now evaluated acute dynamic changes in rat breast tumors.

Rats bearing syngeneic subcutaneous (*n* = 15) or orthotopic (*n* = 7) 13762NF breast tumors were exposed to a 16% O_2 gas breathing challenge and monitored using blood oxygen level dependent (BOLD) R_2* and tissue oxygen level dependent (TOLD) T_1-weighted measurements at 4.7 T. As a control, we used a traditional hyperoxic gas breathing challenge with 100% O_2 on a subset of the subcutaneous tumor bearing rats (*n* = 6). Tumor subregions identified as responsive on the basis of R_2* dynamics coincided with the viable tumor area as judged by subsequent H&E staining. As expected, R_2* decreased and T_1-weighted signal increased in response to 100% O_2 breathing challenge. Meanwhile, 16% O_2 breathing elicited an increase in R_2*, but divergent response (increase or decrease) in T_1-weighted signal. The T_1-weighted signal increase may signify a dominating BOLD effect triggered by 16% O_2 in the relatively more hypoxic tumors, whereby the influence of increased paramagnetic deoxyhemoglobin outweighs decreased pO_2. The results emphasize the importance of combined BOLD and TOLD measurements for the correct interpretation of tumor oxygenation properties.

Graphical Abstract

* Presented in part at the 26th Annual Meeting of International Society for Magnetic Resonance in Medicine, Paris, France, June 2018 and the recipient of an ISMRM Magna Cum Laude Merit Award.

Corresponding Author: Ralph P. Mason, Ph.D., UT Southwestern Medical Center, 5323 Harry Hines Boulevard, Dallas, Texas 75390-9058, Phone: 214-648-8926, Ralph.Mason@UTSouthwestern.edu.

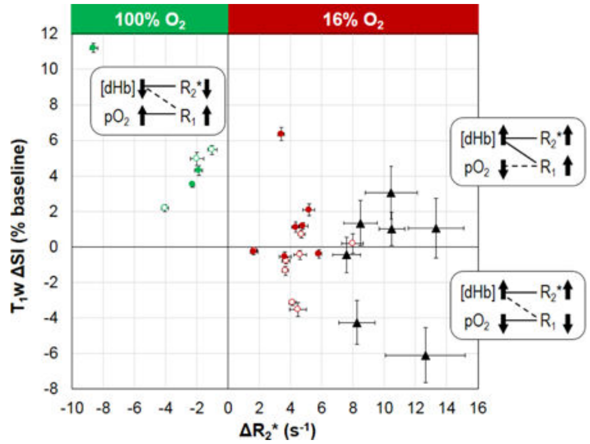

Oxygen-sensitive MRI of 13762NF breast tumors growing subcutaneously or orthotopically in syngeneic rats showed expected opposite R_2* (BOLD) responses to 16% O_2 and 100% O_2 breathing challenges. T_1-weighted signal (TOLD) was consistent with 100% O_2, but showed divergent response (increase or decrease) in response to 16% O_2. In light of R_2* responses as well as pimonidazole staining, we attribute the apparent anomaly to the influence of deoxyhemoglobin on R_1 under hypoxia conditions generating a caveat for interpretation of oxygen-sensitive data.

Keywords

Oxygen; Hypoxic Gas; Hypoxia; BOLD; TOLD; Tumor; Intratumoral Heterogeneity; Rat

INTRODUCTION

Hypoxia has become a key target in cancer therapy development (1). Hypoxia is associated with tumor aggressiveness and resistance to therapy (2–4). Oxygen-sensitive MRI presents potential for characterizing tumor hypoxia and predicting therapeutic efficacy non-invasively (3,5–8). Oxygen-sensitive MRI studies are typically conducted with a hyperoxic gas breathing challenge, such as air to oxygen or carbogen (7–33), especially because alleviating tumor hypoxia via hyperoxic gas breathing has proven beneficial to radiotherapy (7,17,26,34,35). During the time course of a gas breathing challenge, MRI metrics based on spin–lattice relaxation rate constant (R_1) and/or transverse relaxation rate constant (R_2*) are measured to reveal the changes in tumor oxygenation. In a classical scenario, tumor R_1 (or T_1-weighted, T_1w, signal) increases in response to hyperoxic gas breathing, consistent with increased concentration of paramagnetic oxygen molecules and hence oxygen partial pressure (pO_2) in tissue: the tissue oxygen level dependent (TOLD) effect. On the other hand, a decrease in tumor R_2* (or an increase in T_2*-weighted signal) indicates the conversion of deoxy- to oxyhemoglobin and increased blood oxygen saturation (sO_2): the blood oxygen level dependent (BOLD) effect. Distinct relationships have been reported between R_2* and tumor oxygenation based on polarographic electrodes, fiber optic probes, ^{19}F MRI and immunohistochemistry assays (36–38), but while specific correlates have been observed there are often trends rather than direct correlations. Indeed, vasoactive agents may alter vascular volume and hence the amount of deoxyhemoglobin within a tumor (more specifically imaging voxel), causing apparently contrary response in R_2* (11).

R_1 in solution is linearly dependent on the concentration of free oxygen molecules and hence pO_2 (18,27,39,40). In well-defined media such as vitreous humor and cerebrospinal fluid R_1 may reliably measure pO_2, but many additional factors influence relaxation including macromolecules, pH and temperature. Nonetheless a change in R_1 with respect to an acute intervention such as oxygen breathing challenge is expected to indicate change in pO_2. However, apparently contradictory R_1 responses to hyperoxic gas breathing have been reported, *i.e.*, decrease or minimal change in R_1 (or T_1w signal) (7,8,30,41,42). This apparently contradictory R_1 response is denoted as the "alternative" TOLD response in the following context. The most popular hypothesized mechanism underlying this alternative TOLD response is the infiltration of a blood oxygenation effect on R_1, since deoxyhemoglobin is itself paramagnetic (7,8,30,41,42). Indeed, in vascular regions the conversion of deoxyhemoglobin to oxyhemoglobin may reduce R_1, while ultimately, O_2 is released into the tissue enhancing R_1. The direction of R_1 response in a voxel depends on the balance of these two processes. This effect has been thoroughly investigated in blood samples (43–45). We have now sought to better characterize this seemingly contradictory MRI behavior in tumors by examining their acute response to a hypoxic gas breathing challenge.

To better characterize the apparently contradictory TOLD response, we evaluated tumor response to a hypoxic gas (16% O_2) breathing challenge using oxygen-sensitive MRI, and compared it to the classical 100% O_2 breathing challenge. We hypothesized that by reducing the fraction of inspired oxygen, tumors would exhibit this alternative TOLD response. Therefore, MR metrics accompanying hypoxic gas breathing should not simply "mirror" the effect of hyperoxic gas breathing. There have been few previous reports of MRI with respect to hypoxic gas (< 21% O_2) challenge, predominantly in the brain or brain tumors (27,46–49) and recently placenta (28) and abdominal tissues (50) and apparently none comparing dynamic BOLD and TOLD response in tumors.

EXPERIMENTAL

Investigations were approved by the Institutional Animal Care and Use Committee.

Animal preparation

Rat mammary adenocarcinoma 13762NF tissue (originally obtained from the Division of Cancer Treatment and Diagnosis, National Cancer Institute, Bethesda, MD, USA) was implanted subcutaneously in the right thigh (n = 15) or orthotopically in the lower right mammary fat pad (n = 7) of adult female Fischer 344 rats (~125–200 g; Charles River Laboratories, Wilmington, MA, USA). Briefly, a donor rat was anaesthetized via inhalation of a mixture of isoflurane (2–3%) and oxygen and the right hind limb was shaved. A thawed piece of frozen 13762NF tissue, measuring approximately 2 × 2 × 2 mm^3, was inserted subcutaneously into a small incision (approximately 0.5–1 cm long) on the outer thigh of the right hind limb. The skin was closed using wound clips (9 mm). After 7 to 10 days, the incision site had healed and the clips were removed. The donor tumor was allowed to grow to 1–1.5 cm in diameter before it was excised and pieces implanted subcutaneously into the thigh or in the orthotopic mammary fat pad of no more than four recipient rats.

Subcutaneous (SC) tumors were allowed to grow to small (0.2–1.5 cm^3) and large (2.5–6 cm^3) volumes for MRI experiments. A subset of SC tumors (3 small and 3 large) was subjected to a hyperoxic gas breathing challenge using 100% O_2 (gbc100). On the following day, all SC tumors (8 small and 7 large) were subjected to a hypoxic gas breathing challenge using 16% O_2 (gbc16). Meanwhile, orthotopic (OT) tumors grew faster so only large (2.5–6 cm^3) volumes were available for MRI experiments upon the release of rats from surgery recovery. The OT tumors were subjected to only gbc16. On the following day, ten SC tumors (5 small and 5 large) and four OT tumors were excised for histology. The procedures performed for each tumor are specified in Table 1.

MRI with gas breathing challenge

MRI was performed using a horizontal bore 4.7 T system (Agilent/Varian, Santa Clara, CA, USA). Each tumor-bearing rat was anesthetized using isoflurane (typically, 2.5% for induction and at a specific concentration in the range 1.75–2.25% during MRI, with constant breathing gas flow rate at 2 L/min). Isoflurane was chosen since it is reported to have minimal effect on pO_2 and BOLD MRI signal in tumors and skeletal muscles (51). Warm air and a circulating water blanket were used to maintain the body temperature at 36–37 °C. For SC tumors, the tumor-bearing limb was placed inside a lab-made, single-turn volume solenoid radiofrequency coil (25-mm diameter). For OT tumors, the rat was placed inside a Litzcage coil (Model DSI-1366, Doty Scientific, Columbia, SC, USA). Physiological parameters, including body (rectal) temperature, respiration rate, and peripheral oxygen saturation (s_pO_2; measured on the forearm), were recorded during MRI using a monitoring system (Model 1030; Small Animal Instruments, Stony Brook, NY, USA). To minimize potential effects of varying environmental factors on rat physiology, isoflurane concentration was kept constant throughout the MRI session for each rat. Breathing gas flow rate (2 L/min), circulating water temperature (45 °C), and rat placement on the MRI platform (including position, orientation, taping location and tightness) were kept consistent across different MRI sessions. Medical air (21% O_2) was used during baseline measurements, and then the breathing gas was switched to either 100% or 16% O_2 (balance N_2). Each gas was delivered via a nose cone directly from a commercial container (Airgas, Radnor Township, PA, USA) without further mixing except with isoflurane.

Two T_2-weighted (T_2w) anatomical scans were acquired using a fast spin-echo sequence. The first scan covered the whole tumor volume with 15 to 35 slices without gap, depending on tumor size (transaxial view; slice thickness: 1 mm for SC tumors; 2 mm for OT tumors), which was used for image planning and tumor volume calculation. The second scan selected a target slice that captured the largest cross section of the tumor with 2 mm thickness. Other parameters were: TR = 3 s, echo train length of 8, effective TE = 64 ms, k-space size 128 × 128, field of view 25 × 25 or 30 × 30 mm^2 for SC tumors and 70 × 70 mm^2 for OT tumors, 4 averages, and scan time of 3 min 12 s. The spatial planning of this target slice was transferred onto all following measurements.

Images for R_2, R_1, R_2* (BOLD), and T_1-weighted (TOLD) measurements were acquired with k-space size 128 × 64, generating raw in-plane resolution of 0.20 × 0.40 or 0.23 × 0.46 mm^2 for SC tumors and 0.55 × 1.1 mm^2 for OT tumors, depending on the field of view. Zero-filling was applied to the phase-encoding direction, which resulted in a k-space size of 128 × 128 and the corresponding in-plane resolution was 0.20 × 0.20 or 0.23 × 0.23 mm^2 for SC tumors and 0.55 × 0.55 mm^2 for OT tumors. R_2 measurements used a Carr-Purcell-Meiboom-Gill (CPMG) sequence with TR = 2 s, 15 TEs ranging from 20 to 300 ms in increments of 20 ms, 2 averages, 20 dummy scans, and scan time of 4 min 56 s. R_1 measurements used the modified fast inversion-recovery (MFIR) method (52) integrated with a slice-selective inversion pulse and a segmented turboFLASH acquisition (53). The scan parameters were: inversion-recovery TR = 6 s, TI = 0.01, 0.35, 1.4, 3.1, 5.5 s (quadratically spaced (54)), 4 averages, and scan time of 8 min. During each inversion-recovery TR, 16 k-space lines were acquired with the following parameters: 10° flip angle, acquisition TR = 10 ms, and TE = 5 ms.

BOLD and TOLD measurements were interleaved, with 20 acquisitions during baseline and 20 accompanying challenge gas. BOLD measurements were acquired as R_2* maps using a multi-gradient-echo sequence with transverse-magnetization spoiling (TR = 150 ms, TE ranging from 5 to 100 ms for SC tumors and 5 to 80 ms for OT tumors in increments of 5 ms, 20° flip angle, 4 averages, 20 dummy scans, and scan time of 41 s). TOLD measurements were acquired as T_1-weighted (T_1w) images using a gradient-echo sequence with transverse-magnetization spoiling (TR = 30 ms, TE = 5 ms, 45° flip angle, 8 averages, 20 dummy scans, and scan time of 16 s). Including the systematic time lag between two sequential scans, the total scan time of the interleaved BOLD and TOLD session was approximately 49 min.

During the anatomical scans and R_2 measurement, the rat typically reached a stable state with body temperature of 37 °C and respiration rate of 40–60 breaths per min. When a rat needed a longer stabilization period (0–30 min), additional R_2 and R_1 maps were acquired. Once the physiology became stable, an R_1 measurement for baseline was acquired and then the interleaved BOLD/TOLD session was initiated. Immediately after BOLD/TOLD scan set #20 (the last baseline acquisition), the breathing gas was switched to the challenge gas. After the completion of BOLD/TOLD scan set #40, another R_1 measurement for challenge gas was acquired.

Histology and immunohistochemistry

Immunohistochemical assessment of hypoxia was conducted in 14 tumors (specified in Table 1). Within 24 hr post MRI, the tumor-bearing rats received intravenous infusion of pimonidazole (60 mg/kg; Hypoxyprobe™-1 Plus Kit; Hypoxyprobe Inc., Burlington, MA, USA). From 20 min before to 45 min after the injection of pimonidazole, the rats were kept awake in a gas chamber supplying air (n = 10) or 16% O_2 (n = 4). Then, the tumors were excised from anesthetized rats and cut in half at the location replicating the MRI target slice. The tumor specimens were rapidly immersed in 4% paraformaldehyde with overnight fixation followed by a series of hydrations within 24 hr, before they were submitted for routine paraffin embedding, sectioning, and H&E staining (Histo Pathology Core, UT

Southwestern). Pimonidazole was stained in 5 μm paraffin sections using a Hypoxyprobe™-1 Plus Kit according to the manufacturer's protocol for paraffin-embedded tissue. Whole mount images were obtained using a Zeiss Axio Scan.Z1 (Zeiss, Peabody, MA, USA).

Data analysis

MRI data were processed using MATLAB R2017a (MathWorks, Natick, MA, USA). Regions of interest (ROIs) were selected based on the T_2w anatomical images (Fig. 1a). Tumor volume was calculated from the multislice anatomical scan. R_1 maps were generated by fitting the inversion-recovery data set (signal intensity, SI, *vs.* TI) on a voxel-by-voxel basis to a three-parameter, mono-exponential model:

$$\mathrm{SI(TI)} = \mathrm{A} - \mathrm{B} \cdot \exp\left(-\mathrm{TI} \cdot \mathrm{R}_1\right). \quad [1]$$

R_2 (from CPMG measurement) and R_2* (from BOLD measurement) maps were generated by fitting the transverse-relaxation data set (SI *vs.* TE) on a voxel-by-voxel basis to a two-parameter, mono-exponential model:

$$\mathrm{SI(TE)} = \mathrm{A} \cdot \exp(-\mathrm{TE} \cdot \mathrm{R}), \quad [2]$$

where R represents R_2 or R_2*.

The T_1-weighted signal intensity (T_1w SI) from TOLD measurements was corrected to remove T_2^*-weighted signal decay as follows:

$$\mathrm{SI} = \mathrm{SI}^{\mathrm{raw}} / \exp\left(-\mathrm{R}_2{}^* \cdot \mathrm{TE}\right), \quad [3]$$

where SI^{raw} is the raw signal intensity prior to correction, TE = 5 ms for all TOLD measurements, and R_2* was determined voxel-by-voxel from the BOLD measurement preceding each TOLD measurement.

To present dynamic parameter changes, R_2* and T_1w SI at each time point were referenced to their corresponding baseline means:

$$\Delta\, \mathrm{R}_2{}^*(t) \equiv \mathrm{R}_2{}^*(t) - \mathrm{R}_2{}^*(\mathrm{baseline}), \quad [4a]$$

$$\Delta\, \mathrm{SI}(t) \equiv \frac{\mathrm{SI}(t) - \mathrm{SI}(\mathrm{baseline})}{\mathrm{SI}(\mathrm{baseline})} \times 100\% \quad , \quad [4b]$$

where t denotes the time of measurement, and R_2*(baseline) and SI(baseline) are the temporal means in each voxel during the designated baseline interval (Eq. 5).

$$P(\text{period}) = \sum_{t \in \text{period}} \frac{P(t)}{n_{\text{period}}}. \quad [5]$$

(period = baseline or challenge)

In Eq. 5, P denotes the parameter of interest (R_2* or T_1w SI) and n_{period} is the number of time points included in a given period interval. In order to allow for physiological stabilization, especially after the change of breathing gas, the baseline and challenge intervals each included the final 60% of time points during the respective gas breathing period (*i.e.*, BOLD/TOLD scan sets 9 to 20 for baseline, and sets 29 to 40 for challenge). In 5 out of 28 MRI experiments, the baseline interval was slightly adjusted to exclude time points acquired when the rats' physiological parameters were unstable, maintaining at least 8 time points for baseline.

When presented without a time index (t), ΔR_2* and T_1w ΔSI denote the difference between the (temporal) means for the gas breathing periods (Eq. 5):

$$\Delta\, R_2^* \equiv R_2^*(\text{challenge}) - R_2^*(\text{baseline}) \quad [6a]$$

$$\Delta\, \text{SI} \equiv \frac{\text{SI(challenge)} - \text{SI(baseline)}}{\text{SI(baseline)}} \times 100\%. \quad [6b]$$

In the analysis of intratumoral heterogeneity, to characterize tumor response to a challenge gas, the following voxel-by-voxel classification was performed for R_2* and T_1w SI, respectively:

$$|\Delta P| \begin{cases} > 2 \times \text{SD}_{\text{temporal}}(\text{baseline}) & : \text{responsive voxel} \\ \leq 2 \times \text{SD}_{\text{temporal}}(\text{baseline}) & : \text{nonresponsive voxel}, \end{cases} \quad [7]$$

where ΔP denotes ΔR_2* or T_1w ΔSI as defined in Eq. 6, and $\text{SD}_{\text{temporal}}$(baseline) is the temporal standard deviation (SD) for P over the baseline interval. Based on this criterion, each tumor voxel was classified as responsive or nonresponsive (Fig. 2a–e). The responsive fraction was calculated by dividing the number of responsive voxels by that of all tumor voxels. The derived response class assignments were then used to calculate the class-specific ΔR_2* and T_1w ΔSI (Figs. 4–6).

In MRI data processing, two types of data quality thresholds were applied to the relevant data sets: based on signal-to-noise ratio (SNR) or goodness of fit, respectively. The SNR threshold was:

$$\mathrm{SI} \gg 2 \times \mu_{\mathrm{background}}, \quad [8]$$

where SI denotes signal intensity in each voxel and $\mu_{\mathrm{background}}$ is the mean signal intensity in a representative background area that did not enclose any subject or apparent artefact (manually outlined). This criterion recognizes that MRI magnitude signal distribution (Rician) deviates from Gaussian-like to Rayleigh distribution under noisy conditions (SNR < 2) (55). In practice, Eq. 8 corresponds approximately to SNR ≥ 2.5 ($\mu_{\mathrm{background}} \approx \sigma\sqrt{\pi/2}$ for background area; σ being the standard deviation of Gaussian noise (55)). For R_1 measurements, the fitting result for a voxel was passed on to further analysis only if the inversion-recovery data set (signal intensity, SI *vs.* TI) in that voxel had at least 3 (out of 5) data points above the SNR threshold (Eq. 8). For R_2 and R_2* measurements, the transverse-relaxation data set (SI *vs.* TE) in each voxel was truncated at the first data point that fell below the SNR threshold (Eq. 8) and only the data points with TE shorter than the cutoff point were used for fitting. The R_2 or R_2* fitting results for a voxel were passed on to further analysis only if the number of included data points was 3 or larger. For TOLD measurements, in each voxel, the dynamic time points that did not meet Eq. 8 were excluded from further analysis.

The goodness of fit was evaluated using the Pearson correlation coefficient (r) between data and model with the P value for testing the hypothesis that there was no relationship between data and model. The goodness-of-fit threshold was: for SC tumors, $r^2 \geq 0.95$ with $p < 0.05$ (for R_1 and R_2 measurements) or $r^2 \geq 0.9$ with $p < 0.05$ (for R_2* measurements due to relatively lower SNR in BOLD data sets); for OT tumors, $r^2 \geq 0.75$ for R_1, R_2, and R_2* measurements (due to relatively lower SNR in OT data sets). For BOLD measurements, fitting result for a voxel was passed on to further analysis only if the data and fit met both the SNR and goodness-of-fit criteria.

Histological images were processed in the Fiji distribution of ImageJ (56). Stain separation was achieved using the Color Deconvolution plugin for ImageJ (57). For the H&E staining, regions of viable tumor and necrotic tissue were identified (Fig. 2f and h). Viable tumor fraction was calculated by dividing the viable tumor area by the whole tumor area. Pimonidazole stained regions within the viable tumor regions were identified (Fig. 2g and i). The hypoxic fraction was calculated by dividing the pimonidazole stained area by the viable tumor area.

Student's *t*-tests (two-tailed, paired or unpaired, as appropriate) were performed for relevant statistical analyses with significance level $p < 0.05$, unless otherwise specified.

RESULTS

Two weeks after implantation, the volume of SC 13762NF tumors ranged from 0.2 to 1.3 cm^3, and reached 2.6 to 5.1 cm^3 during the third week (except for tumor #8, only reaching a volume of 1.4 cm^3 during the third week; Table 1). MRI and histology are shown for a representative tumor (#12) in Figures 1 and 2. A large necrotic region was identified by H&E staining (Fig. 2f). The center of the necrotic region had visually smaller baseline (air breathing) R_1, R_2, and R_2* values compared to viable tumor regions in the periphery (Fig. 1b–d). Baseline parameter histograms showed extensive overlap between viable and necrotic tumor regions (Fig. 1b–e; right panel), while tumor and muscle were well separated by R_2 (Fig. 1c). Within the viable tumor region, pimonidazole staining indicated a hypoxic fraction of 31%, while the tumor-bearing rat was breathing air (Fig. 2g and i). The tumor BOLD response map based on R_2* time course (Fig. 2d) had a spatial pattern matching the tissue type map based on H&E staining (Fig. 2h): responsive voxels resided predominantly in the viable tumor periphery, whereas the nonresponsive voxels were located primarily in the necrotic tumor center. The TOLD response map revealed fewer responsive voxels compared to BOLD with responsive fractions 30% and 53%, respectively, Fig. 2e and d).

Representative time courses of BOLD and TOLD parameters ($\Delta R_2^*(t)$ and T_1w $\Delta SI(t)$, respectively) during gbc100 and gbc16 are shown in Figure 3 together with respiration rate and s_pO_2 (tumor #7). Both rat and tumor physiology appeared stable during the air breathing baseline (Fig. 3). Intervention generated rapid response in s_pO_2 generally yielding a new stable value within 1 min. For this rat gbc100 caused s_pO_2 to increase from 83 ± 3 % to 96 ± 3 % ($p < 0.001$; values representing the highlighted periods in Fig 3), while the respiration rate initially decreased and then returned to the same level as air breathing (42 ± 2 bpm for air breathing; 42 ± 3 bpm for oxygen breathing; $p = 0.32$; Fig. 3a). For gbc16, s_pO_2 decreased from 83 ± 4 % to 56 ± 4 % ($p < 0.001$), while the respiration rate remained constant (52 ± 2 bpm for air breathing; 51 ± 2 bpm for 16% O_2 breathing; $p = 0.15$; Fig. 3b). Temperature was stable within 36–37 °C (gbc100: 36.3 ± 0.0 °C for air breathing *vs.* 36.8 ± 0.1 °C for oxygen breathing, $p < 0.001$; gbc16: 36.1 ± 0.1 °C for air breathing *vs.* 35.9 ± 0.1 °C for 16% O_2 breathing, $p < 0.001$). Characteristics and MRI parameters for individual tumors are presented in Table 1.

BOLD responsive area was found to correlate with the viable tumor area identified by H&E stain in SC tumors (Fig. 4a). Both the BOLD responsive fraction and the viable tumor fraction decreased with increasing tumor volume (Fig. 4b). Based on the pimonidazole staining, hypoxic fraction within the viable tumor regions of the SC tumors was 36 ± 11% ($n = 6$) for air breathing, and significantly greater (58 ± 17%; $n = 4$; $p < 0.05$) for the rats breathing 16% O_2. A correlation was observed between the T_1w ΔSI for gbc16 and the pimonidazole-based hypoxic fraction for tumors harvested while rats breathed 16% O_2 ($r^2 > 0.9$; Supplementary Fig. S1). There was no correlation for those harvested while rats breathed air. Pimonidazole staining was found to be highly consistent between nearby slices (Supplementary Fig. S2 and Table S1).

Recognizing the association of BOLD responsive voxels to the viable tumor regions (Figs. 2 and 4a), parameter responses were classified as presented in Figure 5 and Table 1. Upon respiratory challenge with 16% O_2 the BOLD responsive voxels showed significant R_2* increase in all tumors (n =15) and significant change in T_1w SI in 9 of 15 tumors (Table 1). With respect to the oxygen breathing challenge, the BOLD responsive voxels showed significant R_2* decrease and T_1w SI increase in all tumors (n = 6) (Table 1). For each volume category (small and large), the parameter changes triggered by 16% and 100% O_2 were significantly different ($p < 0.05$; Fig. 5). In the BOLD responsive regions mean R_2* increased for gbc16 (small tumors: +4.4 ± 1.7 s^{-1}; large tumors: +4.1 ± 1.4 s^{-1}) and decreased for gbc100 (small tumors: −2.4 ± 1.5 s^{-1}; large tumors: −4.3 ± 3.8 s^{-1}). The T_1w SI increased for gbc100 (small tumors: +4.2 ± 1.8%; large tumors: +6.3 ± 4.2%). Remarkably, gbc16 triggered a binary T_1w response: decreased T_1w SI in small tumors (−1.1 ± 1.5%; *e.g.*, Fig. 3b), but increased T_1w SI in large tumors (+1.4 ± 2.4%). Histograms demonstrating the voxel-by-voxel T_1w response for individual tumors are shown in Supplementary Figure S3. A typical time course of BOLD and TOLD parameters for a tumor exhibiting apparently contradictory T_1w response with gbc16 is shown in Supplementary Figure S4. In this particular tumor (#10), there was some initial instability, which settled after about 12 min and then all parameters remained stable until the switch of breathing gas to 16% O_2. R_2* responded rapidly appearing similar to the tumor in Figure 3, while the T_1w signal increased gradually, but significantly ($p < 0.001$). Responses of R_2* and T_1w SI in individual tumors to the gas challenges are compared in Figure 6, together with the proposed contributing factors. For gbc100, tumor responses were confined to the upper-left quadrant (R_2* decreased; T_1w SI increased). For gbc16, the responses spread across both upper-right and lower-right quadrants (R_2* increased; binary response in T_1w SI, sensitive to tumor volume).

To extend the study with more biological relevance to breast cancer, we also examined a cohort of 13762NF tumors growing in the lower mammary fat pad. The OT tumors grew faster reaching a mean volume of 3.9 ±1.3 cm^3 in 15 days, compared with 0.8 ± 0.4 cm^3 in 15 days and 3.4 ± 0.9 cm^3 in 21 days for the SC tumors. Extensive central necrosis was observed for both tumor sites (Supplementary Fig. S5). The OT tumors developed a necrotic fraction of 46 ± 10 % (n = 4), similar to the SC (30 ± 15 %; n = 10). MRI parametric images also showed intratumoral heterogeneity for OT tumors (Supplementary Fig. S5), similar to SC tumors. Baseline R_1 and R_2 in OT tumors were significantly greater than SC ($p < 0.05$). The OT and SC tumors shared a similar pattern with respect to the BOLD and TOLD responses to hypoxic gas breathing, with larger magnitude of responses for OT tumors (Fig. 6).

R_1 measurements required relatively long scan time and were implemented mainly for validating the T_1w results. A strong correlation was found between the responses of T_1w SI and R_1 to gas breathing challenge (Supplementary Fig. S6) when analyzing the closest TOLD time points to the adjacent R_1 measurements. The binary response to gbc16 was also observed for ΔR_1 data (Table 1), although ΔR_1 data may be affected baseline drifting in some tumors (Supplementary Fig. S4). While we focused on the acute response to gas breathing challenge, longitudinal stability over a longer time frame may also be important. For those SC tumors undergoing both gbc100 and gbc16 we compared the air-breathing baseline measurements on consecutive days. There were no significant differences in mean values for the groups of tumors: R_1(day 1) = 0.49 ± 0.04 s^{-1} *vs.* R_1(day 2) = 0.52 ± 0.08 s^{-1}

(p = 0.40, unpaired t-test; p = 0.29, paired t-test) and R_2*(day 1) = 44.0 ± 8.4 s^{-1} *vs.* R_2*(day 2) = 47.8 ± 11.6 s^{-1} (p = 0.53, unpaired t-test; p = 0.33, paired t-test). A distinct correlation was observed between ΔR_1 with respect to gbc100 *vs.* gbc16 (r^2 = 0.71). ΔR_2* showed no similar correlation (r^2 = 0.09), but if a single measurement (tumor #9) was eliminated as outlier then r^2 = 0.77.

DISCUSSION

The primary goal of this study was to explore the oxygen-sensitive MRI response of tumors to hypoxic gas breathing challenge. BOLD and TOLD measurements were successfully performed on both SC and OT rat 13762NF breast tumors. BOLD response showed increased R_2* consistent with conversion of oxy- to deoxyhemoglobin accompanying 16% O_2 breathing challenge, which mirrored the response to 100% O_2 breathing challenge. Meanwhile, the TOLD response showed the expected increase in T_1w signal (and R_1) with 100% O_2, but binary behavior with 16% O_2, whereby T_1w signal decreased in some tumors but increased in others.

In common with previous reports, the rat 13762NF tumor model was found to develop extensive central necrosis (36,58–60), which replicates the pathological feature in many clinical cases of primary breast cancer (61). Intratumoral heterogeneity is an important factor to be considered in the analysis and interpretation of tumor MRI data. Subregion-based parameters may provide a more comprehensive and accurate representation of tumor characteristics compared to whole-tumor average parameters (8,27,62–65). Manually drawn ROIs may attempt to differentiate the viable and necrotic regions (based on the visual contrast provided by the static parameter maps; Fig. 1b–e, left panel), but the histograms of these regions overlapped (Fig. 1b–e, right panel). An alternative approach examined the intratumoral heterogeneity in oxygenation response by classifying voxel-wise time courses of BOLD and TOLD parameters (Fig. 2b–e). The response classification based on the BOLD contrast (Fig. 2d) showed similarity with H&E staining (Fig. 2h; Fig. 4a). If a voxel was classified as BOLD responsive, it indicates that the voxel had access to vascular perfusion. On the other hand, the response classification based on the TOLD contrast is subject to the net balance between local oxygen supply and consumption (5,18,30). Indeed, the TOLD responsive area (Fig. 2e) was smaller than the BOLD responsive area (Fig. 2d, e). The correlation between the BOLD responsive area and the viable tumor area identified by H&E staining (Fig. 4a) shows the connection between the (vascular) functional heterogeneity and the biological/pathological heterogeneity, consistent with a recent report regarding rat subcutaneous C6 gliomas (63). Based on this correlation, the BOLD response map was used as a filter to select the perfused responsive tumor regions. Both the BOLD responsive fraction and viable tumor fraction decreased with increasing tumor volume (Fig. 4b).

Necrotic regions have been identified using diffusion methods (ADC and IVIM) based on the intrinsic tissue water properties (66,67) or DCE MRI based on the intravenous infusion of gadolinium contrast agents (8,68,69). BOLD contrast has been compared to the non-model-based DCE parameters and showed similar capability of imaging vasculature (48) and revealing intratumoral heterogeneity (63,70). Potential advantages of using BOLD response to classify intratumoral heterogeneity include: 1) BOLD response relates directly to tumor oxygenation (36); 2) BOLD measurements can be interleaved with TOLD measurements for a single gas breathing intervention, avoiding the need for an additional scanning sequence such as DCE or IVIM; 3) avoiding the need for exogenous gadolinium contrast agents, which have become controversial for routine use (71).

Tumors were found to be distinctly heterogeneous with regional differences in MR parameters at baseline (Fig. 1). Local heterogeneity was also observed with respect to gas breathing challenge: some regions (voxels) showed significant response to intervention whereas others remained essentially unchanged (Fig. 2). When voxels were clustered based on parametric response to each intervention (Figs. 3 and S1), R_2* showed a biphasic response to each gas with an initial rapid component over the first minute, reflecting well perfused arteriolar components, followed by a slower phase which continued for several minutes (Fig. 3). This is similar to the observation in this tumor type based on near-infrared spectroscopy of hemoglobin saturation accompanying a gas breathing challenge (67,72). The magnitude of R_2* response for gbc16 was generally larger than that for gbc100 (Figs. 3, 5, and 6), although gbc16 made a relatively smaller change in the inspired oxygen fraction (f_iO_2). This "asymmetrical" R_2* response has also been reported for rat abdominal organs (50), mouse placenta and fetus (28). Due to the nonlinear (sigmoidal) shape of the oxygen-hemoglobin dissociation curve, the change in local deoxyhemoglobin concentration ([dHb]) in the blood depends not only on the magnitude of change in f_iO_2 but also on the local, baseline oxygenation state (*i.e.*, the location on the dissociation curve). A "downhill" move across the steep portion of the dissociation curve, even triggered by a relatively small change in f_iO_2, may result in a larger change in local [dHb] (and hence R_2*) than an "uphill" move towards the plateau portion of the curve (illustrated in Fig. 1 of (8)). This may be particularly relevant to tumors due to poor oxygen delivery and large oxygen consumption. T_1w signal also showed a biphasic response (Fig. 3).

In this study, the hyperoxic gas breathing challenge (gbc100) served as a reference for the hypoxic gas breathing challenge (gbc16). The BOLD and TOLD responses to gbc100 (Fig. 5) agree with the "classical" observations: increased blood oxygenation (decreased R_2*) and increased tissue oxygenation (increased T_1w SI) (7,8,18,19,22–24,26,27,31). For gbc16, the BOLD response mirrored that observed for gbc100 (Fig. 5a): decreased blood oxygenation (increased R_2*). A similar trend of BOLD response to hypoxic gas breathing was reported for normal abdominal organs (50), placenta (28), and the brain (46). Remarkably, for gbc16, T_1w SI decreased in small SC tumors, but increased in larger SC tumors (Figs. 5b and 6), demonstrating a binary response associated with tumor volume. The basis for TOLD measurements is the dependence of tissue R_1 (and hence T_1w SI) on the concentration of molecular oxygen (an endogenous paramagnetic contrast agent) dissolved in the tissue fluid, $[O_2]$ (5). For the hyperoxic gas breathing challenges, the dominant factor underlying an R_1 increase in tumor is typically the increased tissue pO_2 (proportional to $[O_2]$) (7,8,18,26,27,30) — the classical TOLD effect. Yet, under certain circumstances, the vascular components may also have an observable impact on R_1 in a tumor voxel. Assuming constant hematocrit within the experimental time period, R_1 can be altered by a change in the concentration of the paramagnetic deoxyhemoglobin, which can be considered another facet of BOLD contrast (43–45). This study employed a hypoxic gas breathing challenge, so that the impact of [dHb] on R_1 may be enlarged in the presence of decreased blood sO_2 (increased [dHb]; Figs 5 and 6). For gbc16, the "classical" TOLD response should be decreased T_1w SI (the lower-right quadrant in Fig. 6), signifying decreased pO_2. By contrast, the alternative TOLD response to gbc16 would be increased T_1w SI (the upper-right quadrant in Fig. 6). This alternative response should not be attributed to a hypothetical "increased pO_2", because the oxygen supply was globally reduced (Fig. 4b) and pimonidazole staining verified increased hypoxic fraction from air breathing (36 ± 11%; n = 6) to 16% O_2 breathing (58 ± 17%; n = 4). These data indicate the importance of combining BOLD and TOLD measurements for the correct interpretation of tumor oxygenation properties.

Rapidly interleaved BOLD and TOLD measurements allowed monitoring of baseline stability and filtering out the highly unstable portion of baseline for data analysis. Some animals showed initial instability of both systemic physiological and BOLD and TOLD parameters, but once the baseline parameters stabilized they remained consistent until the intervention (Fig. S4). In 5 out of 28 MRI sessions, the baseline interval for BOLD and TOLD data analysis was slightly adjusted to exclude time points acquired when the rats' physiology was unstable, maintaining at least 8 time points for baseline. While inversion-recovery measurement of R_1 potentially provides higher precision, any artifacts due to baseline instability during the 8-min R_1 measurement could not be readily identified and eliminated. Moreover, any significant drift in R_1 is immediately apparent in the dynamic T_1w time course, but is not obvious when compared with R_1 measured several minutes apart. Therefore, R_1 data were mainly used for validating T_1w measurements in this study (Fig. S6).

In a strict sense, the R_1 and T_1w SI we report could be considered R_1* (apparent R_1) and T_1*w SI due to the "in-flow" effect (73). Change in blood flow and volume can potentially alter the apparent R1 (11,73,74). This factor is often neglected in the simplified modeling of oxygen-sensitive parameters (5). To systematically evaluate the impact of blood flow and volume during gas breathing challenge, one would need to implement perfusion-sensitive methods (75) or flow suppression control (76), which was beyond the scope of this study. R_1 is also sensitive to changes in temperature (~3% per ^{o}C *vs.* 0.1% per Torr (18,42)) and thus it is crucial to maintain stable animal temperature. Here most animals showed stable rectal temperature within 1 ^{o}C over the 50 min experimental time course. Five TI values were used for R_1 measurements in order to limit the scan time. If a longer scan time were feasible, bi-exponential modeling of the inversion-recovery data set could be attempted by acquiring more TI values (*e.g.*, 15–64 TIs (77,78)). Bi-exponential modeling may potentially reveal subtle biophysical factors (*e.g.*, magnetization transfer (77) and intercompartmental water exchange (78)), compared to an apparent R_1 based on mono-exponential modeling, although the correct interpretation of bi-exponential components is often challenging.

CONCLUSION

To explore tumor response to hypoxic gas breathing, oxygen-sensitive MRI was conducted in subcutaneous and orthotopic rat 13762NF tumors. The subcutaneous cohort served as a benchmark for investigating factors contributing to the MRI observations, which included the use of hyperoxic gas as the control. The orthotopic cohort was included to expand the study with more biological relevance to breast cancer. Despite the difference in growth rate, both tumor sites were associated with similar patterns regarding necrosis formation and MRI responses to hypoxic gas breathing. BOLD responses behaved as expected with both hyperoxic and hypoxic gas breathing challenges, whereas TOLD responses were apparently contradictory in many tumors undergoing hypoxic gas breathing challenge (increased, instead of decreased, T_1w signal), attributable to the increase in paramagnetic deoxyhemoglobin exceeding the loss of paramagnetic oxygen. The current results provide a caveat for interpreting oxygen-sensitive MRI and indicate the importance of combining BOLD and TOLD approaches.

Supplementary Material

Refer to Web version on PubMed Central for supplementary material.

ACKNOWLEDGEMENTS

We thank the Histo Pathology Core (John Shelton) for assistance and the Whole Brain Microscopy Facility (supported by the Texas Institute for Brain Injury and Repair) in the Department of Neurology and Neurotherapeutics at UT Southwestern for the access to the Zeiss Axio Scan.Z1. This work was funded in part by CPRIT RP140399 in collaboration with Drs. Kevin G. Pinney and Mary Lynn Trawick at Baylor University and the UT Southwestern Small Animal Imaging Resource, Simmons Comprehensive Cancer Center and AIRC supported by NIH 1P30 CA142543, P41 EB015908 and an ARRA stimulus supplement to 1U24 CA126608.

REFERENCES

1. Wilson WR, Hay MP. Targeting hypoxia in cancer therapy. Nat Rev Cancer 2011;11:393–410. [PubMed: 21606941]
2. Tatum JL, Kelloff GJ, Gillies RJ, et al. Hypoxia: Importance in tumor biology, noninvasive measurement by imaging, and value of its measurement in the management of cancer therapy. International Journal of Radiation Biology 2006;82:699–757. [PubMed: 17118889]
3. Colliez F, Gallez B, Jordan BF. Assessing Tumor Oxygenation for Predicting Outcome in Radiation Oncology: A Review of Studies Correlating Tumor Hypoxic Status and Outcome in the Preclinical and Clinical Settings. Front Oncol 2017;7:10. [PubMed: 28180110]
4. Brown JM, William WR. Exploiting tumour hypoxia in cancer treatment. Nat Rev Cancer 2004;4:437–447. [PubMed: 15170446]
5. Remmele S, Mason RP, O’Connor JPB. MRI Hypoxia Measurements. Functional Imaging in Oncology: Springer Berlin Heidelberg; 2014.
6. Horsman MR, Mortensen LS, Petersen JB, Busk M, Overgaard J. Imaging hypoxia to improve radiotherapy outcome. Nat Rev Clin Oncol 2012;9:674–687. [PubMed: 23149893]
7. Hallac RR, Zhou HL, Pidikiti R, Song K, Stojadinovic S, Zhao DW, Solberg T, Peschke P, Mason RP. Correlations of Noninvasive BOLD and TOLD MRI with pO2 and Relevance to Tumor Radiation Response. Magn Reson Med 2014;71:1863–1873. [PubMed: 23813468]
8. O’Connor JPB, Boult JKR, Jamin Y, et al. Oxygen-Enhanced MRI Accurately Identifies, Quantifies, and Maps Tumor Hypoxia in Preclinical Cancer Models. Cancer Res 2016;76:787–795. [PubMed: 26659574]
9. Karczmar GS, River JN, Li J, Vijayakumar Z, Goldman Z, Lewis MZ. Effects of Hyperoxia on T2* and Resonance Frequency Weighted Magnetic-Resonance Images of Rodent Tumors. NMR Biomed 1994;7:3–11. [PubMed: 8068523]
10. Robinson SP, Rodrigues LM, Ojugo AS, McSheehy PM, Howe FA, Griffiths JR. The response to carbogen breathing in experimental tumour models monitored by gradient-recalled echo magnetic resonance imaging. Br J Cancer 1997;75:1000–1006. [PubMed: 9083335]

11. Howe FA, Robinson SP, McIntyre DJO, Stubbs M, Griffiths JR. Issues in Flow and Oxygenation Dependent Contrast (Flood) Imaging of Tumours. NMR Biomed 2001;14:497–506. [PubMed: 11746943]
12. Dunn JF, O'Hara JA, Zaim-Wadghiri Y, Lei H, Meyerand ME, Grinberg OY, Hou H, Hoopes PJ, Demidenko E, Swartz HM. Changes in oxygenation of intracranial tumors with carbogen: a BOLD MRI and EPR oximetry study. J Magn Reson Imaging 2002;16:511–521. [PubMed: 12412027]
13. Al-Hallaq HA, Fan X, Zamora M, River JN, Moulder JE, Karczmar GS. Spectrally inhomogeneous BOLD contrast changes detected in rodent tumors with high spectral and spatial resolution MRI. NMR Biomed 2002;15:28–36. [PubMed: 11840550]
14. Robinson SP, Rijken PF, Howe FA, McSheehy PM, van der Sanden BP, Heerschap A, Stubbs M, van der Kogel AJ, Griffiths JR. Tumor vascular architecture and function evaluated by non-invasive susceptibility MRI methods and immunohistochemistry. J Magn Reson Imaging 2003;17:445–454. [PubMed: 12655584]
15. Thomas CD, Chenu E, Walczak C, Plessis MJ, Perin F, Volk A. Morphological and carbogen-based functional MRI of a chemically induced liver tumor model in mice. Magn Reson Med 2003;50:522–530. [PubMed: 12939760]
16. Zhao DW, Constantinescu A, Chang CH, Hahn EW, Mason RP. Correlation of tumor oxygen dynamics with radiation response of the Dunning prostate R3327-HI tumor. Radiat Res 2003;159:621–631. [PubMed: 12710873]
17. Rodrigues LM, Howe FA, Griffiths JR, Robinson SP. Tumor R2* is a prognostic indicator of acute radiotherapeutic response in rodent tumors. J Magn Reson Imaging 2004;19:482–488. [PubMed: 15065173]
18. Matsumoto K, Bernardo M, Subramanian S, Choyke P, Mitchell JB, Krishna MC, Lizak MJ. MR assessment of changes of tumor in response to hyperbaric oxygen treatment. Magnet Reson Med 2006;56:240–246.
19. O'Connor JPB, Naish JH, Parker GJM, et al. Preliminary Study of Oxygen-Enhanced Longitudinal Relaxation in MRI: A Potential Novel Biomarker of Oxygenation Changes in Solid Tumors. Int J Radiat Oncol 2009;75:1209–1215.
20. O'Connor JP, Naish JH, Jackson A, et al. Comparison of normal tissue R1 and R*2 modulation by oxygen and carbogen. Magn Reson Med 2009;61:75–83. [PubMed: 19097212]
21. Muller A, Remmele S, Wenningmann I, et al. Intracranial tumor response to respiratory challenges at 3.0 T: impact of different methods to quantify changes in the MR relaxation rate R2*. J Magn Reson Imaging 2010;32:17–23. [PubMed: 20578006]
22. Winter JD, Akens MK, Cheng HL. Quantitative MRI assessment of VX2 tumour oxygenation changes in response to hyperoxia and hypercapnia. Phys Med Biol 2011;56:1225–1242. [PubMed: 21285489]
23. Burrell JS, Walker-Samuel S, Baker LC, Boult JK, Jamin Y, Halliday J, Waterton JC, Robinson SP. Exploring DR_2* and DR1 as imaging biomarkers of tumor oxygenation. J Magn Reson Imaging 2013;38:429–434. [PubMed: 23293077]
24. Remmele S, Sprinkart AM, Muller A, et al. Dynamic and Simultaneous MR Measurement of R1 And R2* Changes During Respiratory Challenges for the Assessment of Blood and Tissue Oxygenation. Magnet Reson Med 2013;70:136–146.
25. Colliez F, Neveu MA, Magat J, Cao Pham TT, Gallez B, Jordan BF. Qualification of a noninvasive magnetic resonance imaging biomarker to assess tumor oxygenation. Clin Cancer Res 2014;20:5403–5411. [PubMed: 25208881]
26. White DA, Zhang Z, Li L, Gerberich J, Stojadinovic S, Peschke P, Mason RP. Developing oxygen-enhanced magnetic resonance imaging as a prognostic biomarker of radiation response. Cancer Lett 2016;380:69–77. [PubMed: 27267808]
27. Beeman SC, Shui YB, Perez-Torres CJ, Engelbach JA, Ackerman JJH, Garbow JR. O2-Sensitive MRI Distinguishes Brain Tumor Versus Radiation Necrosis in Murine Models. Magnet Reson Med 2016;75:2442–2447.
28. Avni R, Golani O, Akselrod-Ballin A, Cohen Y, Biton I, Garbow JR, Neeman M. MR Imaging-derived OxygenHemoglobin Dissociation Curves and Fetal-Placental OxygenHemoglobin Affinities. Radiology 2016;280:68–77. [PubMed: 26780539]

29. Bane O, Besa C, Wagner M, Oesingmann N, Zhu H, Fiel MI, Taouli B. Feasibility and reproducibility of BOLD and TOLD measurements in the liver with oxygen and carbogen gas challenge in healthy volunteers and patients with hepatocellular carcinoma. J Magn Reson Imaging 2016;43:866–876. [PubMed: 26417669]
30. Cao-Pham TT, Joudiou N, Van Hul M, Bouzin C, Cani PD, Gallez B, Jordan BF. Combined endogenous MR biomarkers to predict basal tumor oxygenation and response to hyperoxic challenge. NMR Biomed 2017;30.
31. Zhou H, Zhang Z, Denney R, Williams JS, Gerberich J, Stojadinovic S, Saha D, Shelton JM, Mason RP. Tumor physiological changes during hypofractionated stereotactic body radiation therapy assessed using multi-parametric magnetic resonance imaging. Oncotarget 2017;8:37464–37477. [PubMed: 28415581]
32. Zhou H, Hallac RR, Yuan Q, et al. Incorporating Oxygen-Enhanced MRI into Multi-Parametric Assessment of Human Prostate Cancer. Diagnostics 2017;7:1–15.
33. Neeman M, Dafni H, Bukhari O, Braun RD, Dewhirst MW. In vivo BOLD contrast MRI mapping of subcutaneous vascular function and maturation: validation by intravital microscopy. Magn Reson Med 2001;45:887–898. [PubMed: 11323816]
34. Overgaard J Hypoxic radiosensitization: Adored and ignored. J Clin Oncol 2007;25:4066–4074. [PubMed: 17827455]
35. Kaanders JH, Pop LA, Marres HA, Bruaset I, van den Hoogen FJ, Merkx MA, van der Kogel AJ. ARCON: experience in 215 patients with advanced head-and-neck cancer. Int J Radiat Oncol Biol Phys 2002;52:769–778. [PubMed: 11849800]
36. Zhao D, Jiang L, Hahn EW, Mason RP. Comparison of 1H Blood Oxygen Level-Dependent (BOLD) and 19F MRI to Investigate Tumor Oxygenation. Magnet Reson Med 2009;62:357–364.
37. Baudelet C, Gallez B. Current issues in the utility of blood oxygen level dependent MRI for the assessment of modulations in tumor oxygenation. Curr Med Imaging Rev 2005;1:229–243.
38. Al-Hallaq HA, River JN, Zamora M, Oikawa H, Karczmar GS. Correlation of magnetic resonance and oxygen microelectrode measurements of carbogen-induced changes in tumor oxygenation. Int J Radiat Oncol Biol Phys 1998;41:151–159. [PubMed: 9588930]
39. Berkowitz BA, McDonald C, Ito Y, Tofts PS, Latif Z, Gross J. Measuring the human retinal oxygenation response to a hyperoxic challenge using MRI: Eliminating blinking artifacts and demonstrating proof of concept. Magnet Reson Med 2001;46:412–416.
40. Tadamura E, Hatabu H, Li W, Prasad PV, Edelman RR. Effect of oxygen inhalation on relaxation times in various tissues. Jmri-J Magn Reson Im 1997;7:220–225.
41. Linnik IV, Scott ML, Holliday KF, et al. Noninvasive tumor hypoxia measurement using magnetic resonance imaging in murine U87 glioma xenografts and in patients with glioblastoma. Magn Reson Med 2014;71:1854–1862. [PubMed: 23798369]
42. Zhao DW, Pacheco-Torres J, Hallac RR, White D, Peschke P, Cerdan S, Mason RP. Dynamic oxygen challenge evaluated by NMR T-1 and T-2* - insights into tumor oxygenation. NMR Biomed 2015;28:937–947. [PubMed: 26058575]
43. Silvennoinen MJ, Kettunen MI, Kauppinen RA. Effects of hematocrit and oxygen saturation level on blood spin-lattice relaxation. Magn Reson Med 2003;49:568–571. [PubMed: 12594761]
44. Blockley NP, Jiang L, Gardener AG, Ludman CN, Francis ST, Gowland PA. Field Strength Dependence of R1 and R2* Relaxivities of Human Whole Blood to ProHance, Vasovist, and Deoxyhemoglobin. Magnet Reson Med 2008;60:1313–1320.
45. Grgac K, van Zijl PC, Qin Q. Hematocrit and oxygenation dependence of blood ^1H_2O T_1 at 7 Tesla. Magn Reson Med 2013;70:1153–1159. [PubMed: 23169066]
46. Dunn JF, Wadghiri YZ, Meyerand ME. Regional heterogeneity in the brain's response to hypoxia measured using BOLD MR imaging. Magnet Reson Med 1999;41:850–854.
47. Noth U, Kotajima F, Deichmann R, Turner R, Corfield DR. Mapping of the cerebral vascular response to hypoxia and hypercapnia using quantitative perfusion MRI at 3T. NMR Biomed 2008;21:464–472. [PubMed: 17854023]
48. Cai K, Shore A, Singh A, Haris M, Hiraki T, Waghray P, Reddy D, Greenberg JH, Reddy R. Blood oxygen level dependent angiography (BOLDangio) and its potential applications in cancer research. NMR Biomed 2012;25:1125–1132. [PubMed: 22302557]

49. Cahill LS, Zhou YQ, Seed M, Macgowan CK, Sled JG. Brain sparing in fetal mice: BOLD MRI and Doppler ultrasound show blood redistribution during hypoxia. J Cerebr Blood F Met 2014;34:1082–1088.
50. Ganesh T, Estrada M, Duffin J, Cheng HL. T2* and T1 assessment of abdominal tissue response to graded hypoxia and hypercapnia using a controlled gas mixing circuit for small animals. J Magn Reson Imaging 2016;44:305–316. [PubMed: 26872559]
51. Baudelet C, Gallez B. Effect of anesthesia on the signal intensity in tumors using BOLD-MRI: comparison with flow measurements by Laser Doppler flowmetry and oxygen measurements by luminescence-based probes. Magn Reson Imaging 2004;22:905–912. [PubMed: 15288130]
52. Gupta RK, Ferretti JA, Becker ED, Weiss GH. A Modified Fast Inversion-Recovery Technique for Spin-Lattice Relaxation Measurements. J Magn Reson 1980;38:447–452.
53. Edelman RR, Wallner B, Singer A, Atkinson DJ, Saini S. Segmented TurboFLASH : Method for Breath-Hold MR Imaging of the Liver with Flexible Contrast. Radiology 1990;177:515–521. [PubMed: 2171014]
54. Weiss GH, Ferretti JA. Optimal-Design of Relaxation-Time Experiments. Prog Nucl Mag Res Sp 1988;20:317–335.
55. Gudbjartsson H, Patz S. The Rician Distribution of Noisy Mri Data. Magnet Reson Med 1995;34:910–914.
56. Schindelin J, Arganda-Carreras I, Frise E, et al. Fiji: an open-source platform for biological-image analysis. Nat Methods 2012;9:676–682. [PubMed: 22743772]
57. Ruifrok AC, Johnston DA. Quantification of histochemical staining by color deconvolution. Anal Quant Cytol 2001;23:291–299.
58. Song YL, Constantinescu A, Mason RP. Dynamic Breast Tumor Oximetry: The Development of Prognostic Radiology. Technol Cancer Res T 2002;1:471–478.
59. Zhao DW, Jiang L, Hahn EW, Mason RP. Tumor physiologic response to combretastatin A4 phosphate assessed by MRI. Int J Radiat Oncol 2005;62:872–880.
60. Xia M, Kodibagkar V, Liu H, Mason RP. Tumour oxygen dynamics measured simultaneously by near-infrared spectroscopy and 19F magnetic resonance imaging in rats. Phys Med Biol 2006;51:45–60. [PubMed: 16357430]
61. Maiorano E, Regan MM, Viale G, Mastropasqua MG, Colleoni M, Castiglione-Gertsch M, Price KN, Gelber RD, Goldhirsch A, Coates AS. Prognostic and predictive impact of central necrosis and fibrosis in early breast cancer: results from two International Breast Cancer Study Group randomized trials of chemoendocrine adjuvant therapy. Breast Cancer Res Treat 2010;121:211–218. [PubMed: 19280340]
62. O'Connor JPB, Rose CJ, Waterton JC, Carano RAD, Parker GJM, Jackson A. Imaging Intratumor Heterogeneity: Role in Therapy Response, Resistance, and Clinical Outcome. Clin Cancer Res 2015;21:249–257. [PubMed: 25421725]
63. Xu J, Chen A, Xiao J, Jiang Z, Tian Y, Tang Q, Cao P, Dai Y, Krainik A, Shen J. Evaluation of tumour vascular distribution and function using immunohistochemistry and BOLD fMRI with carbogen inhalation. Clin Radiol 2016;71:1255–1262. [PubMed: 27170218]
64. Tomaszewski MR, Gonzalez IQ, O'Connor JP, Abeyakoon O, Parker GJ, Williams KJ, Gilbert FJ, Bohndiek SE. Oxygen Enhanced Optoacoustic Tomography (OE-OT) Reveals Vascular Dynamics in Murine Models of Prostate Cancer. Theranostics 2017;7:2900–2913. [PubMed: 28824724]
65. Featherstone AK, O'Connor JPB, Little RA, Watson Y, Cheung S, Babur M, Williams KJ, Matthews JC, Parker GJM. Data-driven mapping of hypoxia-related tumor heterogeneity using DCE-MRI and OE-MRI. Magnet Reson Med 2018;79:2236–2245.
66. Sigmund EE, Cho GY, Kim S, Finn M, Moccaldi M, Jensen JH, Sodickson DK, Goldberg JD, Formenti S, Moy L. Intravoxel incoherent motion imaging of tumor microenvironment in locally advanced breast cancer. Magn Reson Med 2011;65:1437–1447. [PubMed: 21287591]
67. Zhao D, Chang CH, Kim JG, Liu H, Mason RP. In vivo near-infrared spectroscopy and magnetic resonance imaging monitoring of tumor response to combretastatin A-4-phosphate correlated with therapeutic outcome. Int J Radiat Oncol Biol Phys 2011;80:574–581. [PubMed: 21345614]

68. Little RA, Jamin Y, Boult JKR, et al. Mapping Hypoxia in Renal Carcinoma with Oxygen-enhanced MRI: Comparison with Intrinsic Susceptibility MRI and Pathology. Radiology 2018:171531.

69. Zhao D, Jiang L, Hahn EW, Mason RP. Continuous low-dose (metronomic) chemotherapy on rat prostate tumors evaluated using MRI in vivo and comparison with histology. Neoplasia 2005;7:678–687. [PubMed: 16026647]

70. Jiang L, Zhao D, Constantinescu A, Mason RP. Comparison of BOLD contrast and Gd-DTPA dynamic contrast-enhanced imaging in rat prostate tumor. Magn Reson Med 2004;51:953–960. [PubMed: 15122677]

71. Lenkinski RE. Gadolinium Retention and Deposition Revisited: How the Chemical Properties of Gadolinium-based Contrast Agents and the Use of Animal Models Inform Us about the Behavior of These Agents in the Human Brain. Radiology 2017;285:721–724. [PubMed: 29155619]

72. Liu H, Song Y, Worden KL, Jiang X, Constantinescu A, Mason RP. Noninvasive investigation of blood oxygenation dynamics of tumors by near-infrared spectroscopy. Appl Opt 2000;39:5231–5243. [PubMed: 18354520]

73. Howe FA, Robinson SP, Rodrigues LM, Griffiths JR. Flow and oxygenation dependent (flood) contrast MR imaging to monitor the response of rat tumors to carbogen breathing. Magn Reson Imaging 1999;17:1307–1318. [PubMed: 10576716]

74. Robinson SP, Collingridge DR, Howe FA, Rodrigues LM, Chaplin DJ, Griffiths JR. Tumour response to hypercapnia and hyperoxia monitored by FLOOD magnetic resonance imaging. NMR Biomed 1999;12:98–106. [PubMed: 10392806]

75. Zhang Z, Yuan Q, Zhou H, Zhao D, Li L, Gerberich JL, Mason RP. Assessment of tumor response to oxygen challenge using quantitative diffusion MRI in an animal model. J Magn Reson Imaging 2015;42:1450–1457. [PubMed: 25866057]

76. Zhou H, Belzile O, Zhang Z, Wagner J, Ahn C, Richardson JA, Saha D, Brekken RA, Mason RP. The effect of flow on blood oxygen level dependent (R2*) MRI of orthotopic lung tumors. Magn Reson Med 2019;In press:10.1002/mrm.27661.

77. Prantner AM, Bretthorst GL, Neil JJ, Garbow JR, Ackerman JJH. Magnetization transfer induced biexponential longitudinal relaxation. Magnet Reson Med 2008;60:555–563.

78. Yang DM, Huettner JE, Bretthorst GL, Neil JJ, Garbow JR, Ackerman JJH. Intracellular water preexchange lifetime in neurons and astrocytes. Magn Reson Med 2018;79:1616–1627. [PubMed: 28675497]

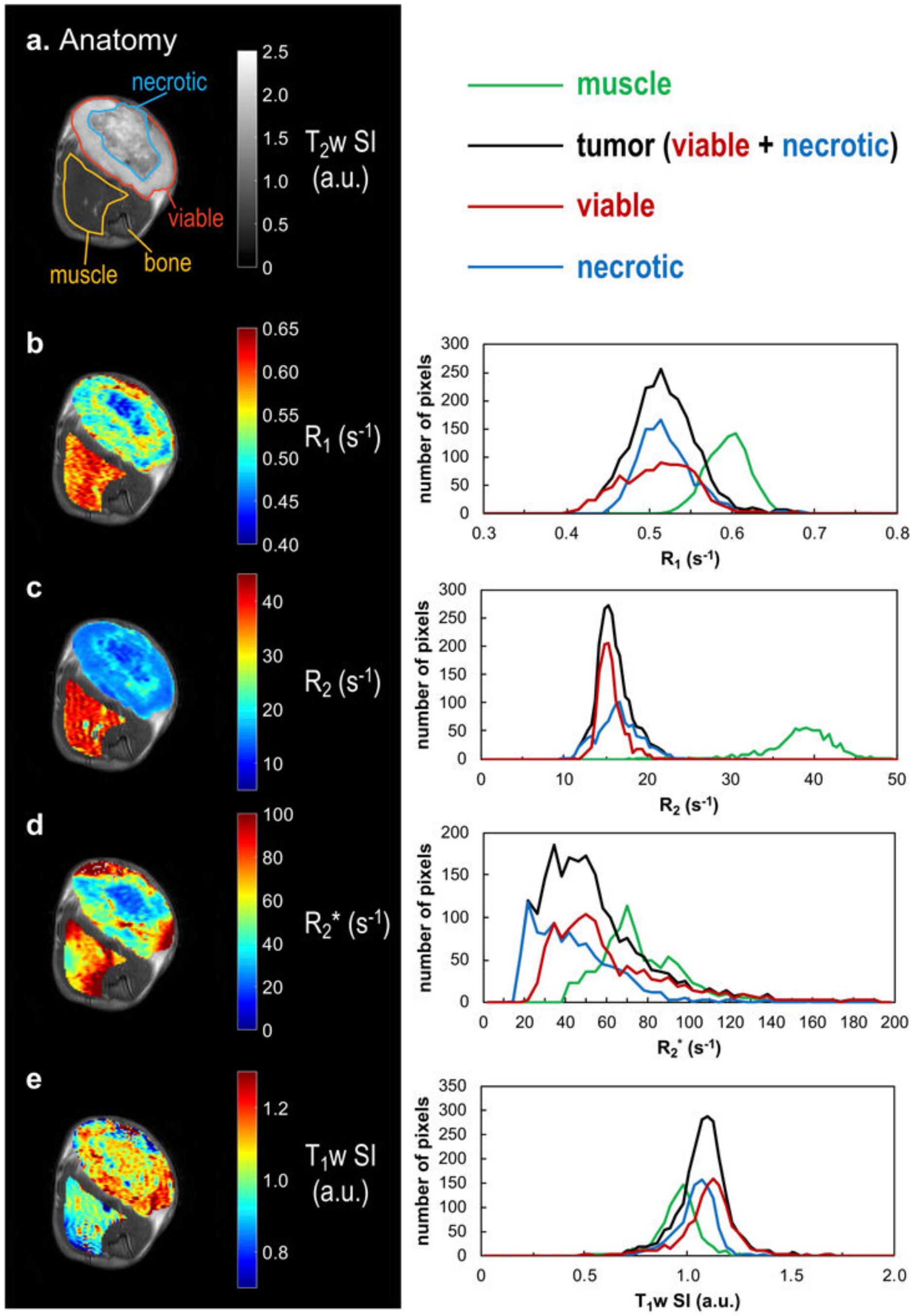

Figure 1. MRI parameter maps and histograms at baseline (air breathing) for a representative subcutaneous 13762NF tumor (#12).

a: T_2w anatomical image with the transaxial view of the tumor-bearing thigh. ROIs were manually selected. Muscle ROI (yellow) was selected excluding the thigh bone region. b–e: maps of baseline R_1, R_2, R_2*, and T_1w SI, respectively (left panel) and the corresponding histograms (right panel). To illustrate the viable and necrotic tumor regions, respectively, the red and blue ROIs (a) were drawn based on the visual contrast in the parameter maps (b–e) with reference to the H&E staining (Fig. 2f).

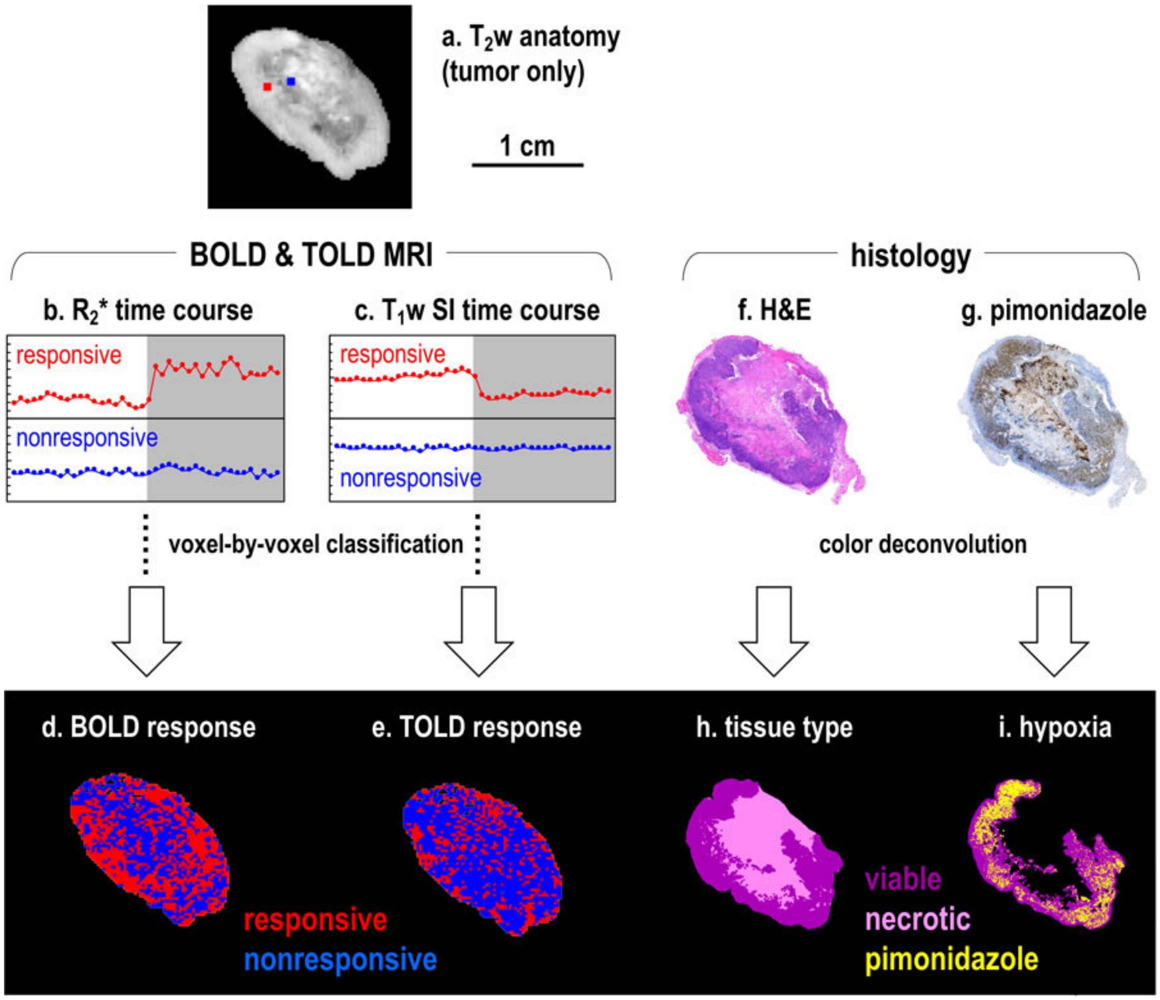

Figure 2. Data processing procedure (illustrated for the same tumor as in Fig. 1).

a: T_2w anatomical image of the tumor. Two representative voxels were chosen (red and blue squares) to demonstrate the procedure of voxel-by-voxel response classification (for better visualization, the square is 8 times larger than the actual voxel). The red voxel was classified as responsive based on the R_2* (b) or the T_1w SI (c) time course, while the blue voxel was classified as nonresponsive. The maps of (d) BOLD and (e) TOLD response were derived using the (b) R_2* and (c) T_1w SI classifications, respectively. Histological images (f and g) were converted to tissue type map (h; viable tumor in magenta; necrotic tissue in pink) and hypoxia map (i; pimonidazole stained regions in yellow) based on color deconvolution. Pimonidazole stain in the necrotic regions (g) was excluded (based on the tissue type map; h) from the hypoxia map (i). For this tumor, pimonidazole was administered while the rat breathed air (Table 1).

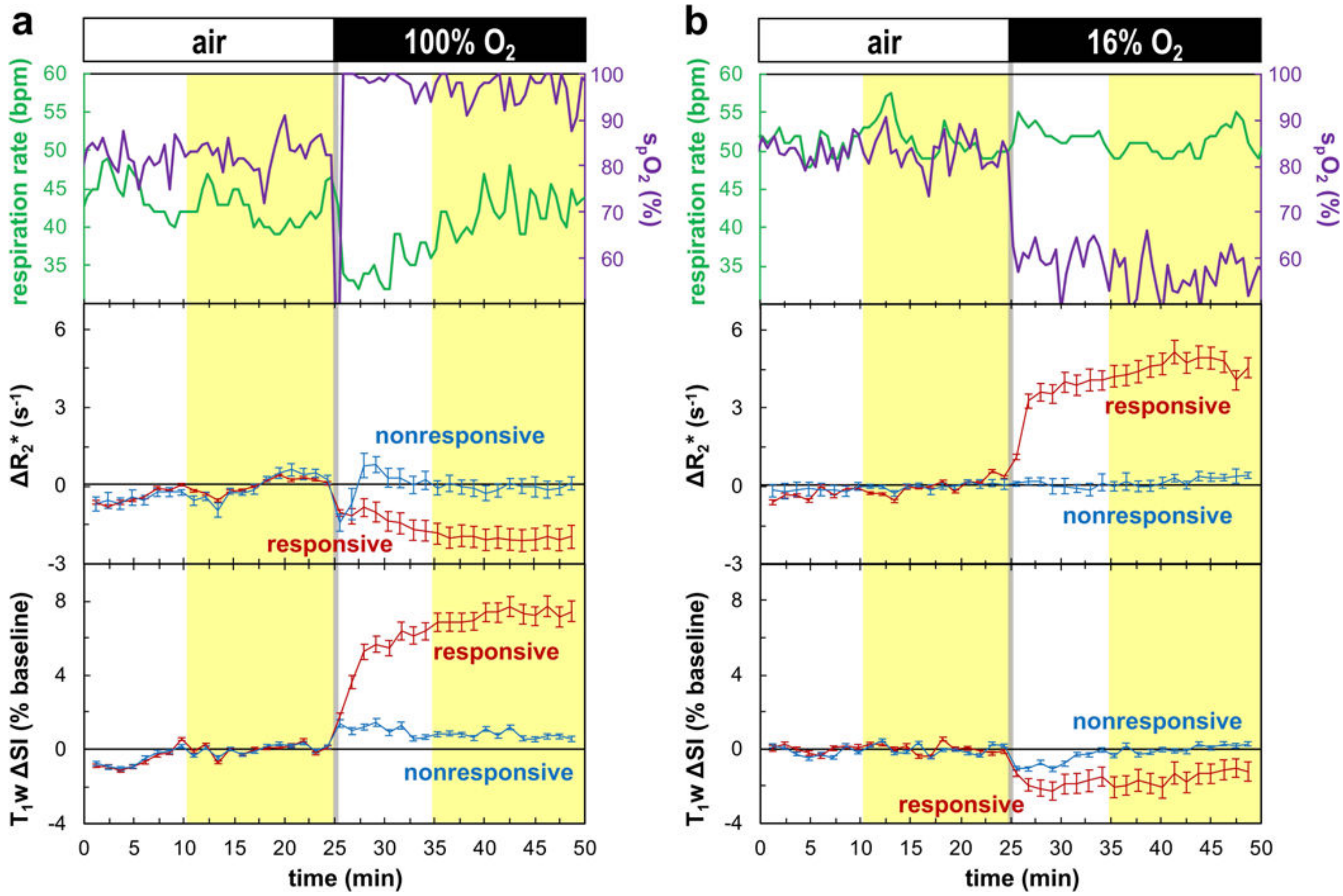

Figure 3. Time courses of oxygen-sensitive parameters with respect to gas breathing challenge using (a) 100% O_2 and (b) 16% O_2 (subcutaneous tumor #7).

Top row: physiological parameters (respiration rate (green); peripheral arterial oxygen saturation, s_pO_2, on the forearm (purple)); middle row: $\Delta R_2^*(t)$ (Eq. 4a); bottom row: T_1w $\Delta SI(t)$ expressed as percentage of baseline (Eq. 4b). The time courses for responsive (red) and nonresponsive (blue) classes are shown separately (mean ± SEM at each time point), based on the BOLD and TOLD classification, respectively (Eq. 7; Fig. 2). The designated baseline and challenge intervals (Eq. 5) are highlighted in yellow. Data within these intervals were used to calculate the mean parameter changes (Eq. 6; Figs. 5 and 6). Switch of gas is marked by the gray vertical lines.

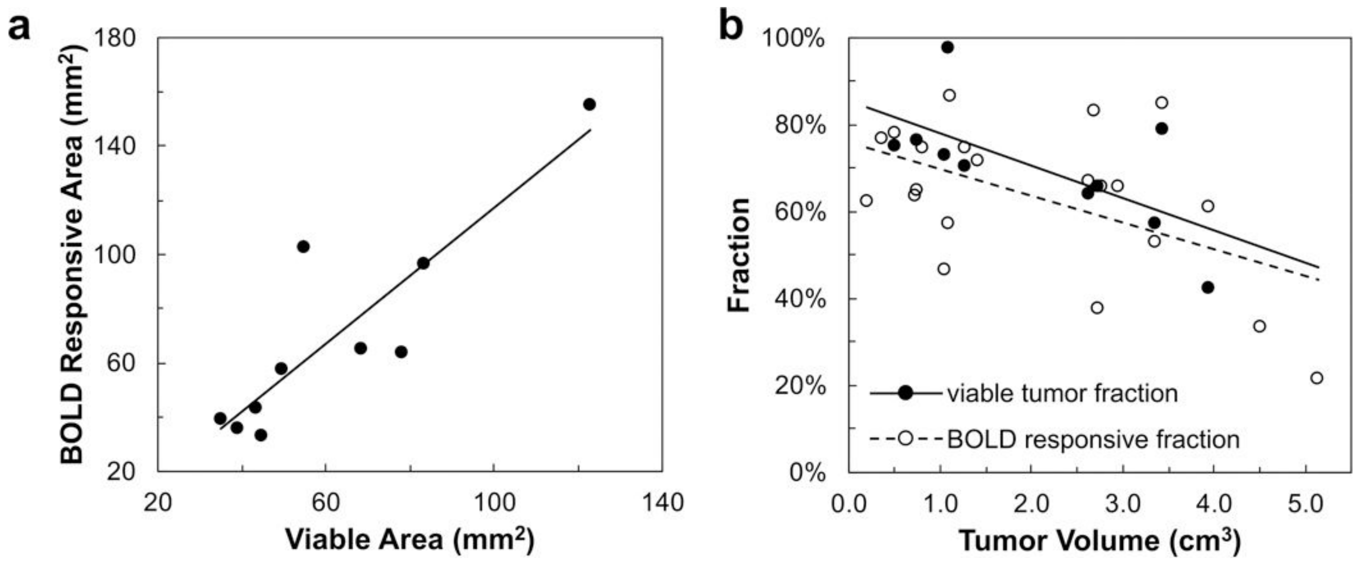

Figure 4. Comparison of BOLD MRI and H&E staining in subcutaneous 13762NF tumors.

a: Significant correlation was observed between the viable tumor area identified by H&E stain and BOLD responsive area ($r^2 = 0.78$; $p < 0.001$). The plot shows the BOLD results from gbc16 experiment performed the day before histology ($n = 10$; Table 1). b: Significant correlations were observed between viable tumor fraction (filled circles; $r^2 = 0.43$; $p < 0.05$) or BOLD responsive fraction (open circles; $r^2 = 0.27$; $p < 0.05$) and tumor volume. BOLD responsive fractions include those determined with gbc16 ($n = 15$) and gbc100 ($n = 6$).

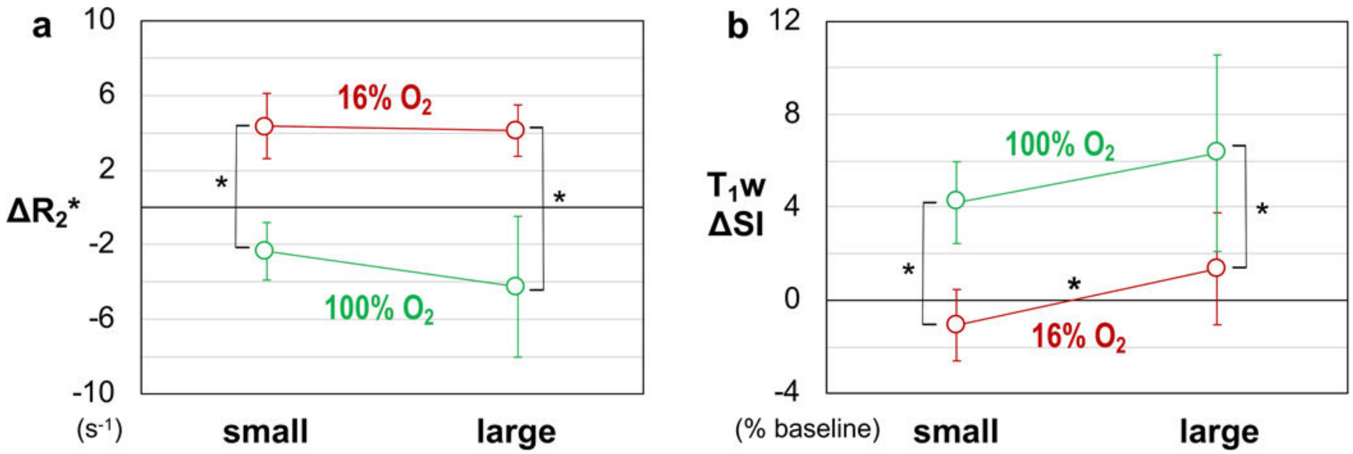

Figure 5. Mean ΔR_2^* (a) and T_1w ΔSI (b) associated with the BOLD responsive regions in subcutaneous tumors.

Values are shown as group mean ± SD, according to the type of challenge and volume category. Asterisks mark significant difference ($p < 0.05$) between groups.

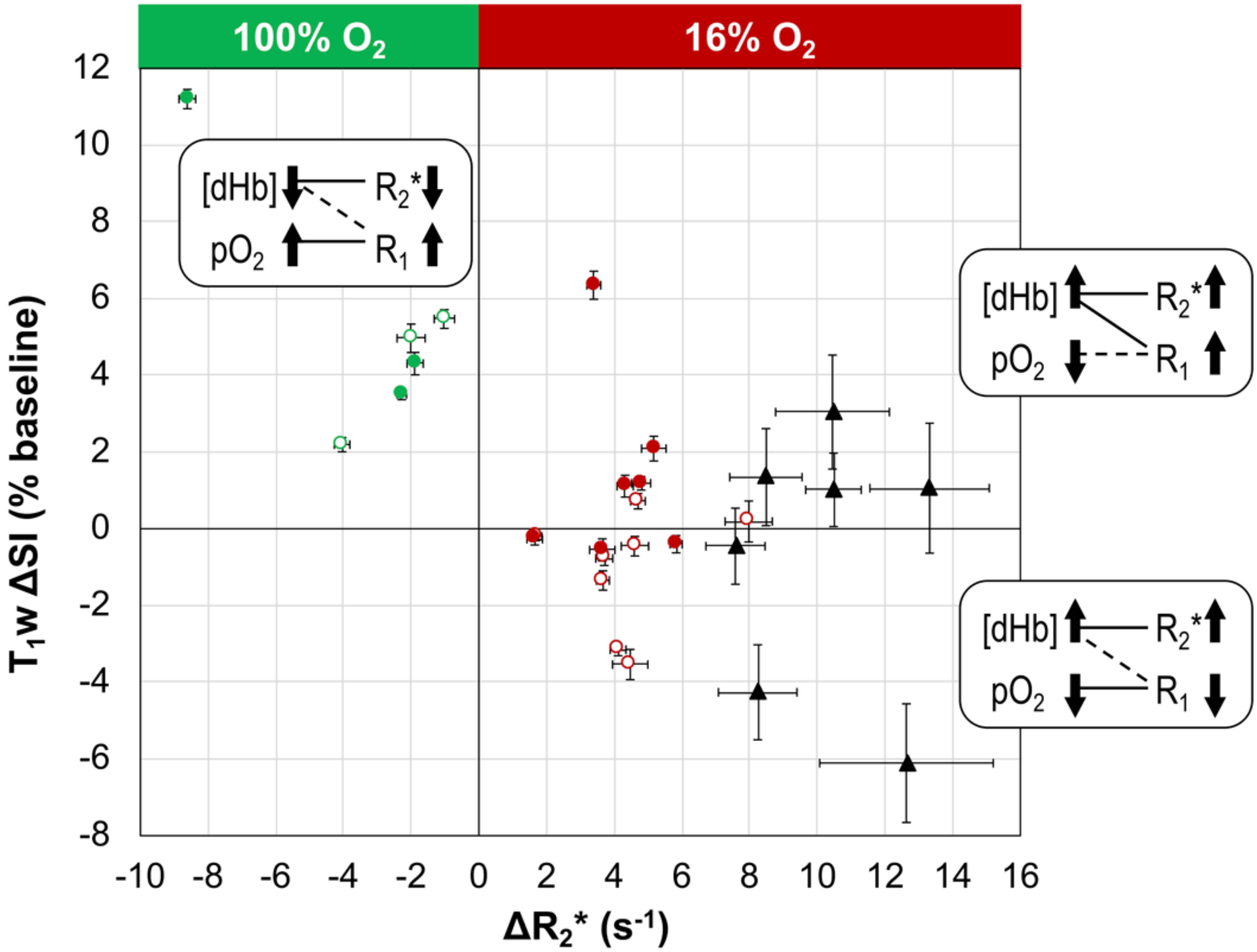

Figure 6. Two-parameter oxygenation profile for individual tumors.

Each tumor is located according to the ΔR_2* and T_1w ΔSI values (mean ± SEM) associated with the BOLD responsive voxels. Data points are labeled according to tumor location and challenge type: open circles for small SC tumors; filled circles for large SC tumors; red circles for gbc16; green circles for gbc100; black triangles for OT tumors in the lower mammary fat pad (gbc16). Proposed contributing factors ([dHb] and pO_2) underlying the tumor responses are given in the corresponding quadrants. The solid connecting lines indicate the dominating factor, while the dashed connection lines indicate the minor factor.

Table 1.

MR parameters (mean ± SEM, unless otherwise specified).

ID	tumor volume (cm^3)	R_2 (s^{-1})	R_1 (s^{-1})		ΔR_1 (s^{-1})	BOLD responsive fraction (%)	ΔR_2^* (s^{-1})		T_1w ΔSI (% baseline)	
							challenge − air		challenge − air	
		air	air	challenge [c]	challenge – air [d]		responsive [d]	nonresponsive [d]	responsive [d]	nonresponsive [d]
small subcutaneous tumors with gbc16 (*n* = 8)										
1	0.2	13.3 ± 0.2	0.525 ± 0.003	0.512 ± 0.003**	−0.013 ± 0.001***	62	4.5 ± 0.5***	0.3 ± 0.1*	−3.5 ± 0.4***	−4.5 ± 0.4***
2	0.4	12.8 ± 0.1	0.496 ± 0.002	0.513 ± 0.002***	0.017 ± 0.001***	77	3.7 ± 0.2***	0.8 ± 0.2**	−1.3 ± 0.3***	−2.2 ± 0.3***
3[a]	0.5	13.3 ± 0.1	0.516 ± 0.003	0.520 ± 0.003	0.004 ± 0.002	78	8.0 ± 0.7***	−0.3 ± 0.2	0.2 ± 0.5	−1.8 ± 0.8
4[b]	0.8	11.9 ± 0.1	0.471 ± 0.002	0.489 ± 0.002***	0.017 ± 0.001***	65	4.1 ± 0.2***	0.3 ± 0.1***	−3.2 ± 0.2***	−3.2 ± 0.2***
5[b]	1.1	8.7 ± 0.1	0.432 ± 0.020	0.408 ± 0.001	−0.023 ± 0.020	46	3.7 ± 0.3***	0.3 ± 0.1**	−0.8 ± 0.2***	0.4 ± 0.1**
6[a]	1.1	11.4 ± 0.1	0.631 ± 0.052	0.587 ± 0.042	−0.026 ± 0.033	57	1.7 ± 0.2***	0.4 ± 0.2*	−0.2 ± 0.1	0.0 ± 0.2
7[a]	1.3	13.2 ± 0.1	0.488 ± 0.002	0.487 ± 0.001	−0.002 ± 0.001	75	4.6 ± 0.4***	0.2 ± 0.2	−0.5 ± 0.3	−0.9 ± 0.3**
8	1.4	12.2 ± 0.1	0.479 ± 0.001	0.481 ± 0.001	0.002 ± 0.001**	72	4.7 ± 0.2***	0.5 ± 0.1***	0.7 ± 0.2***	−0.1 ± 0.3
group[e]	**0.8 ± 0.4**	**12.1 ± 1.5**	**0.505 ± 0.059**	**0.500 ± 0.050**	**−0.003 ± 0.017**	**66 ± 11**	**4.4 ± 1.7**	**0.3 ± 0.3**	**−1.1 ± 1.5**	**−1.5 ± 1.7**
large subcutaneous tumors with gbc16 (*n* = 7)										
9[b]	2.6	16.2 ± 0.1	0.580 ± 0.021	0.541 ± 0.013	−0.039 ± 0.023	67	5.2 ± 0.4***	−0.1 ± 0.2	2.1 ± 0.3***	2.8 ± 0.4***
10[a]	2.7	14.2 ± 0.1	0.482 ± 0.001	0.482 ± 0.001	0.000 ± 0.001	38	4.3 ± 0.2***	0.3 ± 0.1***	1.1 ± 0.3***	1.2 ± 0.1***
11	2.8	14.7 ± 0.1	0.518 ± 0.001	0.536 ± 0.001***	0.018 ± 0.001***	65	4.8 ± 0.3***	0.5 ± 0.1***	1.2 ± 0.2***	0.9 ± 0.2***
12[a]	3.4	16.0 ± 0.1	0.517 ± 0.001	0.508 ± 0.001***	−0.009 ± 0.001***	53	3.6 ± 0.4***	0.1 ± 0.1	−0.6 ± 0.3	0.2 ± 0.2
13[b]	3.4	11.7 ± 0.1	0.462 ± 0.002	0.488 ± 0.002***	0.026 ± 0.002***	85	5.8 ± 0.2***	−0.2 ± 0.3	−0.4 ± 0.2	−2.0 ± 0.4***
14[a]	4.0	14.4 ± 0.1	0.511 ± 0.010	0.508 ± 0.010	−0.0032 ± 0.0004***	61	1.6 ± 0.2***	0.0 ± 0.1	−0.3 ± 0.2	−0.2 ± 0.1
15	5.1	9.9 ± 0.1	0.430 ± 0.002	0.458 ± 0.002***	0.027 ± 0.001***	21	3.4 ± 0.2***	0.25 ± 0.04***	6.3 ± 0.4***	6.9 ± 0.1***
group[e]	**3.4 ± 0.9**	**13.9 ± 2.3**	**0.500 ± 0.048**	**0.503 ± 0.030**	**0.003 ± 0.023**	**56 ± 21**	**4.1 ± 1.4**	**0.1 ± 0.2**	**1.4 ± 2.4**	**1.4 ± 2.8**
small subcutaneous tumors with gbc100 (*n* = 3)										

ID	tumor volume (cm^3)	R_2 (s^{-1})	R_1 (s^{-1})		ΔR_1 (s^{-1})	BOLD responsive fraction (%)	ΔR_2^* (s^{-1})		T_1w ΔSI (% baseline)	
							challenge − air		challenge − air	
		air	air	challenge [c]	challenge – air [d]		responsive [d]	nonresponsive [d]	responsive [d]	nonresponsive [d]
3	0.7	13.9 ± 0.1	0.530 ± 0.001	0.535 ± 0.001*	0.005 ± 0.001***	63	−4.0 ± 0.2***	−1.1 ± 0.2***	2.2 ± 0.2***	2.0 ± 0.2***
6	0.8	11.8 ± 0.1	0.484 ± 0.002	0.507 ± 0.002***	0.022 ± 0.001***	75	−1.0 ± 0.3**	−0.1 ± 0.1	5.5 ± 0.2***	5.7 ± 0.4***
7	1.1	14.0 ± 0.1	0.497 ± 0.001	0.536 ± 0.002***	0.039 ± 0.001***	86	−2.0 ± 0.4***	−0.1 ± 0.3	5.0 ± 0.4***	3.3 ± 0.5***
group [e]	**0.9 ± 0.2**	**13.3 ± 1.3**	**0.504 ± 0.024**	**0.526 ± 0.017**	**0.022 ± 0.017**	**75 ± 11**	**−2.4 ± 1.5**	**−0.4 ± 0.6**	**4.2 ± 1.8**	**3.6 ± 1.9**
large subcutaneous tumors with gbc100 (*n* = 3)										
9	2.7	15.0 ± 0.1	0.517 ± 0.015	0.584 ± 0.022*	0.067 ± 0.025**	83	−8.6 ± 0.2***	−0.2 ± 0.2	11.2 ± 0.3***	9.9 ± 0.5***
13	3.0	10.7 ± 0.1	0.480 ± 0.013	0.469 ± 0.003	−0.011 ± 0.012	66	−1.9 ± 0.2***	−0.4 ± 0.1**	4.3 ± 0.3***	3.2 ± 0.2***
15	4.5	9.0 ± 0.1	0.413 ± 0.008	0.416 ± 0.001	0.004 ± 0.007	33	−2.3 ± 0.1***	−0.13 ± 0.03***	3.5 ± 0.1***	2.2 ± 0.1***
group [e]	**3.4 ± 1.0**	**11.6 ± 3.1**	**0.470 ± 0.053**	**0.490 ± 0.086**	**0.020 ± 0.042**	**61 ± 25**	**−4.3 ± 3.8**	**−0.2 ± 0.2**	**6.3 ± 4.2**	**5.1 ± 4.2**
orthotopic tumors in lower mammary fat pad with gbc16 (*n* = 7)										
16 [a]	2.5	22.7 ± 0.3	0.98 ± 0.17	1.28 ± 0.20	0.19 ± 0.17	29	10.5 ± 0.8***	0.8 ± 0.6	1.0 ± 1.0	−1.9 ± 0.5***
17	2.9	10.7 ± 0.1	0.95 ± 0.10	1.08 ± 0.12	0.07 ± 0.09	8	13.3 ± 1.8***	0.2 ± 0.3	1.1 ± 1.7	−2.7 ± 0.4***
18 [a]	3.1	22.5 ± 0.4	0.69 ± 0.09	0.65 ± 0.08	−0.04 ± 0.08	12	12.6 ± 2.6***	0.4 ± 0.4	−6.1 ± 1.5***	−3.1 ± 0.5***
19	3.1	14.5 ± 0.2	0.433 ± 0.004	0.470 ± 0.003***	0.037 ± 0.004***	20	8.5 ± 1.1***	1.6 ± 0.2***	1.3 ± 1.3	−2.7 ± 0.5***
20 [a]	4.8	17.2 ± 0.2	1.10 ± 0.14	0.96 ± 0.12	−0.13 ± 0.09	24	7.6 ± 0.9***	1.6 ± 0.3***	−0.5 ± 1.0	−0.7 ± 0.5
21	4.8	12.7 ± 0.2	0.53 ± 0.04	0.47 ± 0.01	−0.06 ± 0.04	14	8.2 ± 1.2***	1.4 ± 0.5**	−4.3 ± 1.2**	−0.8 ± 0.6
22 [a]	5.9	14.8 ± 0.2	0.75 ± 0.08	0.73 ± 0.08	−0.02 ± 0.08	15	10.4 ± 1.7***	1.0 ± 0.3***	3.0 ± 1.5*	−2.0 ± 0.4***
group [e]	**3.9 ± 1.3**	**16.4 ± 4.7**	**0.78 ± 0.25**	**0.81 ± 0.31**	**0.01 ± 0.10**	**66 ± 12**	**10.2 ± 2.2*****	**1.0 ± 0.5**	**−0.6 ± 3.3**	**−2.0 ± 0.9**

a & **b**: Histology and immunohistochemical assessment of hypoxia (using pimonidazole) was conducted within 24 hr post MRI.

[a]: The rat breathed air with respect to pimonidazole injection.

[b]: The rat breathed 16% O_2 with respect to pimonidazole injection.

[c]**:** Unpaired *t*-tests (challenge *vs.* baseline) for each tumor.

[d]: Paired *t*-tests (challenge *vs.* baseline) for each tumor.

[e]: Group mean ± SD.

* $p < 0.05$

** $p < 0.01$

*** $p < 0.001$.

Author Manuscript
Author Manuscript
Author Manuscript